*High Power Laser Science and Engineering*, (2024), Vol. 12, e79, 9 pages.
doi:10.1017/hpl.2024.55

HIGH POWER LASER SCIENCE AND ENGINEERING

RESEARCH ARTICLE

# High-flux angularly uniform proton beams from multiple laser interaction with wire-hemisphere targets

Xiangrui Jiang[1,2], Debin Zou[1], Mingyang Yu[3], Na Zhao[4], Lixiang Hu[1], Jianming Ouyang[1], Fuqiu Shao[1], Wenhui Tang[2], and Tongpu Yu[1]

[1] *Department of Physics, National University of Defense Technology, Changsha, China*

[2] *Department of Nuclear Science and Technology, National University of Defense Technology, Changsha, China*

[3] *College of Engineering Physics, Shenzhen Technology University, Shenzhen, China*

[4] *School of Microelectronics and Physics, Hunan University of Technology and Business, Changsha, China*

*(Received 14 March 2024; revised 6 August 2024; accepted 20 August 2024)*

**Abstract**

A scheme for generating high-flux angularly uniform proton beams with high laser-to-proton energy conversion efficiency is proposed. Three laser beams are focused on a microwire array attached to a solid-density hemispheric target. The laser-driven hot electrons from the front of the microwire hemisphere generate a hot-electron sheath in the hollow behind it, so that the protons on its back are accelerated by target normal sheath acceleration. The accelerated protons are of high flux, as well as angularly and energetically uniform. The scheme should be useful for applications involving warm dense matter, such as isochoric heating and modification of materials, as well as for proton therapy and inertial confinement fusion.

**Keywords:** angular uniformity; high-flux proton beams; multiple lasers

## 1. Introduction

High-intensity pulsed ion beams are widely used in material-surface engineering, such as surface modification[1], film growth[2] and nanopowder preparation[3], since they can melt, evaporate and ablate the material surface within a very short time[4]. Localized high-temperature and high-density colloidal plasmas can also be produced. The pulse duration of high-intensity ion beams from traditional methods (e.g., by using magnetically insulated ion diodes) is limited to $10-1000$ ns[1]. Many efforts have been devoted to reducing the ion beam duration, as needed for the production of warm dense matter (WDM)[5] and inertial confinement fusion (ICF)[6]. Existing accelerator-based or electrically pulsed ion sources can achieve a pulse duration of $1-10$ ns[7], but undesirable hydrodynamic expansion of materials can still occur during the heating period, and it is difficult to realize isochoric heating. Thus, still shorter pulsed ion beams are needed.

With advances in the chirped pulse[8] and related amplification technologies, the duration of intense laser pulses can be compressed to picoseconds and even femtoseconds. As short-pulse energy triggers, such laser pulses open up the possibility of generating pulsed ion beams as short as ps duration[9–13]. Short (<1 ns) pulsed ion beams are useful for studying fundamental material properties and WDM, especially their equation of state[14] and opacity[15], as well as for fuel heating to assist ignition in ICF[16,17]. In many applications, high-flux ion beams suitably matching the target profile are required in order to heat the materials uniformly and avoid local overheating[18], such that the physical and chemical properties of the material bulk remain unchanged. That is, it is necessary to control the beam characteristics. To increase the beam flux, novel curved and conical target structures that improve beam focusing have been proposed[18–23]. Such shaped targets can be fabricated by three-dimensional (3D) direct laser printing[24] or chemical vapor deposition[25–27]. In addition, target-surface destruction by the laser prepulse can also be reasonably controlled by laser cleaning techniques, especially for ultraintense ultrashort laser pulses[28]. However, the efficiency of laser-to-ion energy conversion[22] and spatial uniformity of the ion beam remain problems.

Correspondence to: D. B. Zou, Department of Physics, National University of Defense Technology, Changsha 410073, China. Email: debinzou@nudt.edu.cn

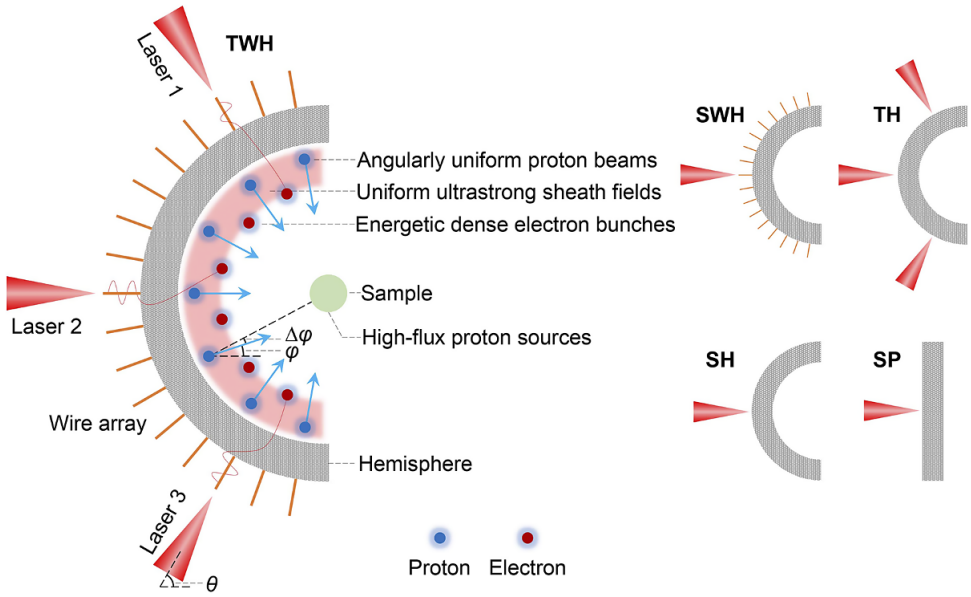


**Figure 1.** Schematic of three laser beams irradiating a wire-hemisphere (left, TWH) target. Four other cases are considered: a single laser beam irradiating a wire-hemisphere (SWH) target, three laser beams irradiating a hemisphere (TH) target, a single laser beam irradiating a hemisphere (SH) target and a single laser beam irradiating a planar (SP) target. The total laser energy is the same in all the five cases.

With novel spatiotemporal synchronization techniques, multiple fs laser beams have recently been used in experiments for improving wakefield electron injection[29] and harmonic generation[30]. The temporal and spatial locations of the laser beams can be controlled to within fs and μm precision by using a motorized stage[29]. That is, one can quite well control laser–plasma interactions involving multiple lasers. In this paper, we propose a scheme for generating high-flux angularly uniform energetic proton beams through target normal sheath acceleration (TNSA) by irradiating a microwire-hemisphere target with three fs laser pulses. Figure 1 is a sketch of the setup. In order to see the effect of the wire array and target curvature, four cases are considered.

## 2. Model and simulation parameters

To verify our scheme, we use the particle-in-cell (PIC) simulation code EPOCH[31]. The two-dimensional (2D) simulation box is $x \times y = 100\lambda_0 \times 120\lambda_0$, with 100 cells per $\lambda_0$ and 36 macroparticles per cell, where $\lambda_0 = 1\,\mu\text{m}$ is the laser wavelength. The outer diameter and thickness of the hemisphere target are $20\lambda_0$ and $3\lambda_0$, respectively. Its material depends on the desired ion beam. For simplicity, we consider a hydrogen plasma target of density $n_e = n_p = 100n_c$, where $n_c = m_e\omega_0^2\varepsilon_0/e^2$ is the critical plasma density, $\omega_0$ is the laser frequency, $\varepsilon_0$ is the vacuum permittivity and $-e$ and $m_e$ are the electron charge and rest mass. For the three laser beams irradiating a wire-hemisphere target (TWH) case, a copper (Cu) nanowire array of density $100n_c$, radius $r_0 = 0.1\lambda_0$ and length $L_0 = 3\lambda_0$ is attached to the front surface of the hemisphere. All wires are oriented toward the center of the hemisphere and are placed with angular uniformity. The angle between two adjacent wires is $\alpha = 10°$. Three p-polarized laser beams incident at angles $\theta = -60°$, $0°$ and $60°$ relative to the $x$ direction are focused on the target front surface. The spatiotemporal profile of each laser beam is $\exp\left[-(r/\sigma_0)^2\right]$ and $\sin^2(\pi t/2\tau_0)$, where $\sigma_0 = 3\lambda_0$ is the focal spot radius, $\tau_0 = 10T_0$ is the pulse duration and $T_0 = 3.3$ fs is the laser cycle. The normalized laser amplitude is $a_0 = eE_0/m_e\omega_0 c = 5.8$, where $E_0$ is the peak electric field strength of the laser and $c$ is the speed of light in vacuum. This corresponds to laser intensity of $4.56 \times 10^{19}$ W/cm$^2$, laser power of 6.4 TW and laser energy of 0.16 J. For the cases with a single laser beam (a single laser beam irradiating a wire-hemisphere target (SWH), a single laser beam irradiating a hemisphere target (SH) and a single laser beam irradiating a planar target (SP)), $a_0 = 10$ is used, so that the total laser energy in the five cases is the same.

## 3. Results and discussion

We record the properties of the protons entering an imaginary (i.e., protons can pass through but not be reflected from it, and nothing happens inside) spherical sample of radius $1\lambda_0$ located at the center of the target-back hollow, as indicated by the green circle in Figure 1. The evolution of the proton flux $\mathcal{F}$ (shadow colored slice profiles) of the five cases is shown in Figure 2(a). One can see that in the TWH case, the peak flux $\mathcal{F}_p$ and total number (i.e., cumulative flux) $\mathcal{N}_t$ of the protons are $1.55 \times 10^{30}$ cm$^{-2}$ s$^{-1}$ and $1.53 \times 10^{16}$, respectively. They are an order of magnitude higher than that of the SP case, and about double or triple that of the SH and TH cases, since the wires lead to higher laser energy absorption efficiency[32] and more uniform laser

https://doi.org/10.1017/hpl.2024.55 Published online by Cambridge University Press

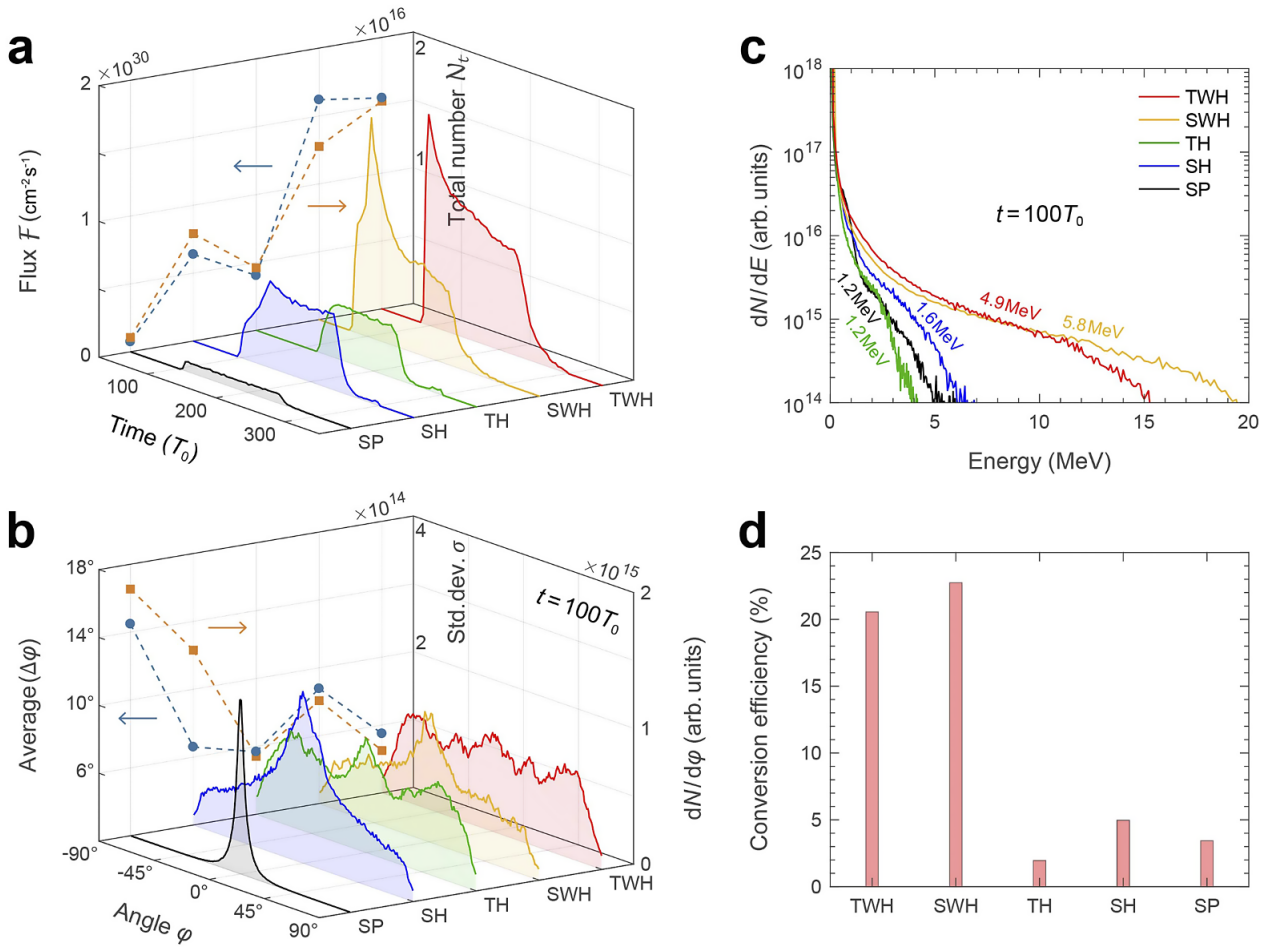


**Figure 2.** (a) Evolution of the TNSA proton flux $\mathcal{F}$ for the five cases in Figure 1. Here, only protons with energies higher than 0.5 MeV are counted. The blue dots and orange squares are for the peak flux $\mathcal{F}_p$ and total number $\mathcal{N}_t$, respectively, of the protons. (b) Angular distributions of the protons behind the targets at $t = 100T_0$. The blue dots and orange squares are for the averaged angular deviation $\langle\Delta\varphi\rangle$ (i.e., the average angle between the momentum direction of each proton and its direction with respect to the target center) of all protons, as well as the standard deviation of the proton angular distribution $\sigma$. For the SP case, the averaged angular deviation, standard deviation and proton number are divided by 2, 4 and 6, respectively. (c) Proton energy spectra at $t = 100T_0$. The proton temperatures (obtained from the gradients of the curves) are also given. (d) The maximum laser-to-proton (with energies higher than 0.5 MeV) energy conversion efficiency $\eta_p$ for the five cases.

intensity distribution on the hemisphere front surface. This includes the contributions of the wire array, laser beamlets and curved structure. Although the single-pulse intensity in the TWH case is only one-third of that in the SWH case, $\mathcal{F}_p$ is comparable and $\mathcal{N}_t$ is even higher than in the SWH case. Moreover, the full-width at half-maximum (FWHM) of $\mathcal{F}$ in the TWH case is twice that of the SWH case, indicating the high $\mathcal{F}$ can remain for an extended time. This is because in the TWH case the spatial uniformity of the three pulses can counteract the loss of the low single-pulse intensity. Figure 2(b) shows the angular distributions of the protons behind the targets at $t = 100T_0$. It is found that for single laser beams the divergence angle of protons is small. With the use of multiple laser beams, the accelerated protons are much more uniformly distributed within $-90° < \varphi < 90°$, where $\varphi$ is the angle of the proton momentum with respect to the $x$ direction (with the anticlockwise direction as positive). For the TH case, one can see that there are three small peaks, corresponding to the three laser beams.

Of interest is that the proton angular distribution in the TWH case is much more uniform than that of the TH case. This is because the most intense part of each beam is on the wires. That is, the wires act like a buffer for the Gaussian lasers, resulting in a significantly more uniform angular distribution of the light intensity. Angular uniformity of the protons can be described by two parameters, namely, the averaged angular deviation $\langle\Delta\varphi\rangle = \sum_{i=1}^{N} |\Delta\varphi_i| / N$ of all protons and the standard deviation of their angular distribution:

$$\sigma = \sqrt{\sum_{i=1}^{q} (N_i - N/q)^2 / q}, \tag{1}$$

where $\Delta\varphi_i$ is the angle between the momentum direction of each proton and the direction of the proton toward the sample

https://doi.org/10.1017/hpl.2024.55 Published online by Cambridge University Press

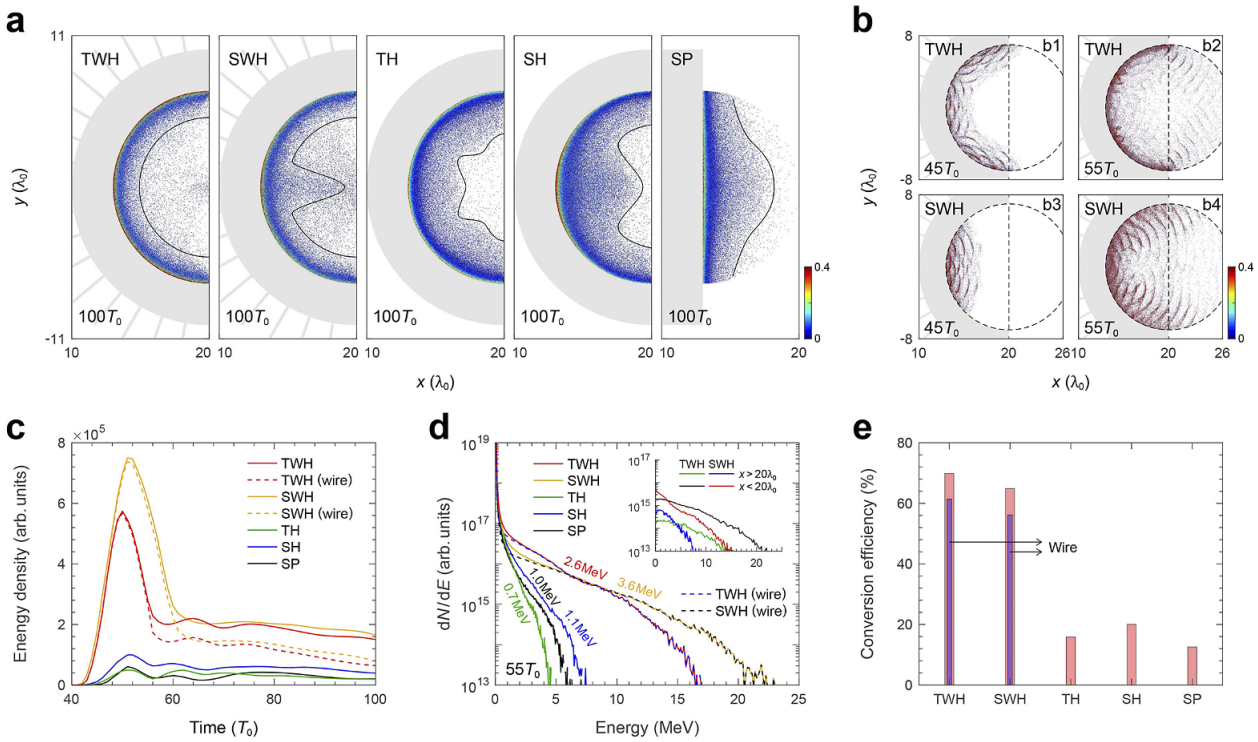


**Figure 3.** (a) Hot-electron energy-density distributions in the region behind the wire-hemisphere structure at $t = 100T_0$. The solid black curve shows a typical constant-energy-density contour relatively far away from its back surface. (b) Energy-density distribution of the wire electrons at $t = 45T_0$ and $55T_0$ for the (b1), (b2) TWH and (b3), (b4) SWH cases, respectively. (c) Evolution of the total electron energy density in the hollow behind the targets. The red and yellow dashed curves are for the contribution of the wire electrons in the TWH and SWH cases. (d) Electron-energy spectra at $t = 55T_0$. The blue and black dashed curves show the spectra of the wire electrons in the TWH and SWH cases. The inset shows the electron energy spectra in the $x > 20\lambda_0$ (green and blue curves) and $x < 20\lambda_0$ (black and red curves) regions of panels (b2) and (b4) for the TWH and SWH cases. (e) Laser-to-electron energy conversion efficiencies. The overlapping inner bars in the TWH and SWH cases are those of the laser-to-wire electrons only, from which one can clearly see the effect of the wires.

center, $N$ is the total number of protons behind the target and $\varphi \in [-90°, 90°]$. We divide this 180° range into $q$ equal parts (here $q = 180$), and the proton number of each part is $N_i$, so that $N = \sum_{i=1}^{q} N_i$. One can see that for the SP case, $\langle \Delta\varphi \rangle$ and $\sigma$ are about 29° and $1.5 \times 10^{15}$, respectively, whereas in the TWH case, they are only 5.5° and $6.2 \times 10^{13}$. That is, in the TWH case a relatively large number of protons can converge toward the sample. Note that the angular uniformity of protons in the TWH case is also obviously better than that of the SWH case. Therefore, the TWH case has significant advantages in producing high-flux and angularly uniform proton beams. The proton spectra at $t = 100T_0$ and laser-to-proton energy conversion efficiencies $\eta_p$ are shown in Figures 2(c) and 2(d). We can see that the TWH setup is also advantageous for enhancing the proton energy. The maximum proton energy $\varepsilon_{p,\,max}$, proton temperature $T_p$ and $\eta_p$ are about 15 MeV, 4.9 MeV and 20.6% (slightly lower than that of the SWH case with high single-pulse intensity), respectively, and for the SP case they are only about 5 MeV, 1.2 MeV and 3.4%, respectively. Note that $\varepsilon_{p,\,max}$ and $\eta_p$ for the TWH and SWH cases are considerably higher than that of the TH, SH and SP cases, indicating the effectiveness of the wire microstructure. Moreover, $\varepsilon_{p,\,max}$ and $\eta_p$ for both the TH and SP cases are lower than that of the SH case. This is because in addition to the curvature of the target, proton acceleration is also affected by the laser intensity[9,10].

Next we consider the causes for the uniform distribution of the generated high-flux proton beams. Figure 3(a) compares the energy-density distribution of the hot electrons behind the five targets at $t = 100T_0$. One can see that in the TWH case, the electrons have much more uniform angular distribution and higher energy density. Figure 3(b) shows the energy-density distributions of electrons from only the wires in the TWH and SWH cases at $t = 45T_0$ and $55T_0$. They are in the form of small periodic beamlets. This is because the dense attosecond electron bunches are pulled out from the surface of metal wires by the transverse electric field of the laser[32,33]. They are then accelerated forward by the ponderomotive force of the laser as well as the longitudinal electric field of a transverse magnetic (TM) mode that is excited in the vacuum channels between the wires[33]. When these electrons pass through the hemisphere, the laser pulse is reflected back by the high-density hemisphere shell. Thus, the electrons continue to move forward in almost the original direction over a short distance of a few micrometers. As these bunches leave the shell, some are well confined near the

https://doi.org/10.1017/hpl.2024.55 Published online by Cambridge University Press

back surface of the shell by the space-charge sheath electric field $E_s$, while others escape from the sheath field and move into the $x > 20\lambda_0$ region. The wire electrons are uniformly distributed in space and are responsible for the angularly uniform sheath fields and the subsequent ion acceleration. In contrast, in the SWH, SH and SP cases, the hot electrons are concentrated mainly in the axial region behind focal spot. Figure 3(c) shows the temporal evolution of the total energy density of all electrons behind the target. We see that at all times the energy density in the TWH case is several times higher than that in the cases of TH, SH and SP. Almost all high-energy-density electrons are from the Cu wires and produced between $t = 40T_0$ and $60T_0$. As shown in Figure 3(d), the highest hot-electron temperature and maximum energy in the TWH case are about 2.6 and 17 MeV, respectively, and most electrons with energy greater than 2 MeV are from the wires. It is important to distinguish the high-energy region of wire electrons in the spectrum. The inset shows the spectra of the electrons in the $x < 20\lambda_0$ and $x > 20\lambda_0$ regions of Figures 3(b2) and 3(b4) for the TWH and SWH cases. In both cases, the electrons at $x > 20\lambda_0$ have a lower temperature and cut-off energy because these electrons lose most of their energies as they escape the sheath field. The electrons trapped in the sheath electric field at $x < 20\lambda_0$ are more energetic because they can also gain energy when reflected back to the hemisphere. Figure 3(e) shows the laser-to-electron energy conversion efficiency $\eta_e$ for the five cases. We see that $\eta_e$ is as high as 70% in the TWH case, which is much higher than that of the other cases. The energy conversion efficiency from the laser to the wire electrons is up to 61%.

Figure 4(a) is for the sheath electric field $E_s$ behind the targets at $t = 50T_0$. We see that the electric fields are directed toward the center region of the hollow. In addition, $E_s$ in the TWH case is stronger than that in the TH case due to the higher sheath-electron temperature, as discussed earlier (recall also that the sheath field of the hot electrons is given by $E_s \propto \sqrt{n_e T_e}$[34]). For completeness, Figure 4(b) shows some typical electric fields at a distance $0.5\lambda_0$ away from the local rear surface of the targets. One can see that the field intensity distribution in the TWH case is generally uniform, with only a few relatively small fluctuations. The uniformity of the sheath fields for TNSA of the target protons can be seen from the standard deviations of their strength distributions:

$$\sigma(E_s) = \sqrt{\sum_{i=1}^{q}\left(E_{s,i} - \sum_{i=1}^{q} E_{s,i}/q\right)^2 /q}, \qquad (2)$$

where $E_{s,i}$ is the field strength at each simulation grid. Figure 4(c) shows $\sigma(E_s)$ for the five cases. We see that the TWH and TH cases have the lowest $\sigma(E_s)$ and thus are the most uniform. Figure 5 shows the energy-density

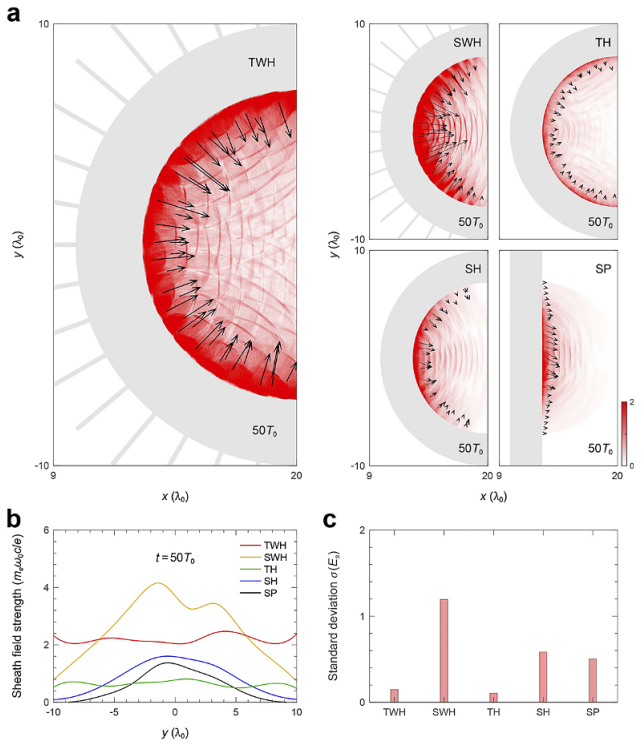


**Figure 4.** (a) Distributions of the electric field strength behind the five targets at $t = 50T_0$. The arrows show the electric field magnitudes and directions. (b) Profiles of the sheath electric field at a distance $0.5\lambda_0$ perpendicular to the local target-rear surface. (c) Standard deviation of the sheath electric fields shown in (b).

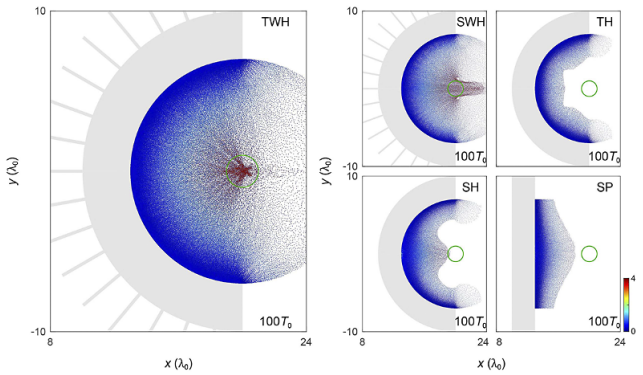


**Figure 5.** Proton energy-density distribution in the circular region behind the five targets at $t = 100T_0$.

distributions of the protons in a circular region behind the target at $t = 100T_0$. As expected, in the TWH case there is a large spot of high-energy-density protons.

It should be noted that the simulation is 2D, which tends to overestimate the hot-electron temperature, resulting in higher proton energy and flux[35,36]. Moreover, the longitudinal electric field of waveguide TM mode in the vacuum regions (no longer channels in three dimensions) between the wires could differ from that of two dimensions and can thus also affect the proton acceleration[33].

https://doi.org/10.1017/hpl.2024.55 Published online by Cambridge University Press

## 4. Parametric effects and experimental considerations

In the TWH case, the effect of proton acceleration is closely related to the geometric parameters of the wire array. Figure 6 shows the dependence of $\mathcal{F}_p$ on the radius $r_0$, length $L_0$ of the wires and angle $\alpha$ between the two adjacent wires. One can see that the TWH case is robust in producing high-flux proton beams over a relatively wide range of wire parameters, as shown in Figure 6(a). For the same $\alpha$, $\mathcal{F}_p$ is higher as $r_0$ becomes smaller since less laser energy is reflected. However, when $r_0$ is fixed, there is an optimal $\alpha$ to provide enough electrons while reducing light reflection. Figure 6(b) shows the peak flux $\mathcal{F}_p$ of protons at different $L_0$ for $\alpha = 10°$ and $r_0 = 0.1\lambda_0$. We find that the optimal length is $L_0 = 3\lambda_0$ to obtain the highest $\mathcal{F}_p$. This is because in this case the interval between the two adjacent wires at the opening is about $2.3\lambda_0$, and the distance between the tip of the wires and the back surface of the hemisphere is $6\lambda_0$. The focusing condition of the electron beams is thus satisfied, so that they are well concentrated on the target-back surface, resulting in more intense sheath electric fields[37]. The optimum parameters $r_0 = 0.1\lambda_0$ and $L_0 = 3\lambda_0$ are also comparable to that in recent experiments[38,39].

Figure 7(a) shows the effect of the laser incident angle $\theta$ on the proton angular distribution and flux for the TWH case. The angles $\theta$ of the upper and lower wires are symmetrically varied. As expected, as $\theta$ is decreased, the proton distribution becomes more like that of the single-laser case SH. As $\theta$ increases, the proton distribution becomes more uniform. However, as shown in Figure 7(b), $\theta$ has little effect on $\mathcal{F}_p$ and $\mathcal{N}_t$. This is because at small incident angles laser interference can enhance the laser field strength[40], which compensates for the deviation in proton uniformity. Due to experimental factors such as laser spot jitter, the actual incident direction of the laser would have angle deviation $\Delta\theta$ and transverse drift $\Delta s$ from the expected direction. Figures 7(c)–7(f) show the influence of $\Delta\theta$ and $\Delta s$ on the angular distribution and flux of the TNSA protons, respectively. We can see that with increasing $\Delta\theta$ and $\Delta s$, the angular uniformity of the proton beam and $\mathcal{F}_p$ decrease slightly, but $\mathcal{N}_t$ remains roughly the same. This indicates that the TWH case is relatively robust in obtaining high-flux angularly uniform proton beams. It is worth noting that the above conclusions are on a small focal spot with 3 μm radius. For a large spot, the influence of $\theta$, $\Delta\theta$ and $\Delta s$ on the angular distribution and flux of protons is relatively weakened.

For higher power laser pulses, it is necessary to consider the damage of the microstructure by the laser prepulses. To see the effect of the pre-expansion preplasma produced by the prepulse, we performed radiation hydrodynamic simulations using FLASH code[41]. The laser prepulse consists of an amplified spontaneous emission (ASE) pedestal and a picosecond exponentially rising leading edge. The pulse shape and intensity of the prepulse are calculated by the laser peak intensity and contrast. The simulations are performed in 2D cylindrical geometry, using the equation-of-state and multi-group opacity tables from PROPACEOS68[42]. FLASH uses an adaptive mesh refinement (AMR) scheme and the coarsest/finest mesh size used is 0.1/0.02 μm in both directions. The Courant–Friedrich–Lewy (CFL) time limit is 0.4. The laser deposition is by 3D ray-tracing projection on the cylindrical domain.

We now consider the effect of the laser power $P$ (from 6.4 TW to 1 PW), with contrast $10^{10}$. Figure 8(a) shows the density distributions of preplasma produced by the prepulse under five different values of $P$ in the TWH case. We see that as $P$ increases, the surface of the wire-hemisphere target is ablated to smooth the sharp boundaries, and more preplasma of overcritical density fills the gaps between the wires. When

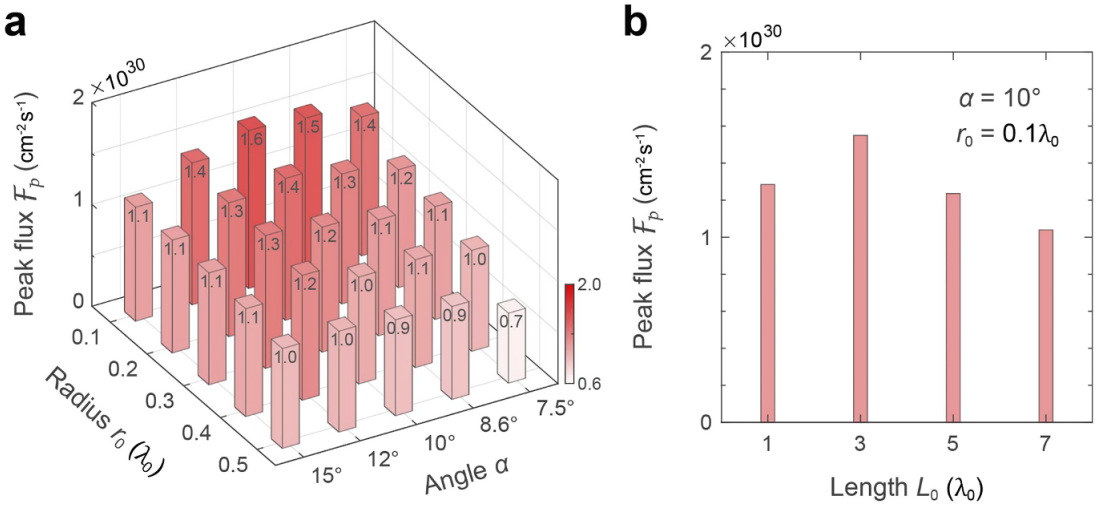


**Figure 6.** Dependence of the peak flux $\mathcal{F}_p$ of protons on (a) the wire radius $r_0$, angle $\alpha$ between the two adjacent wires and (b) wire length $L_0$ in the TWH case. The values (in units of $1 \times 10^{30}$ cm$^{-2}$ s$^{-1}$) marked in (a) are for $\mathcal{F}_p$.

https://doi.org/10.1017/hpl.2024.55 Published online by Cambridge University Press

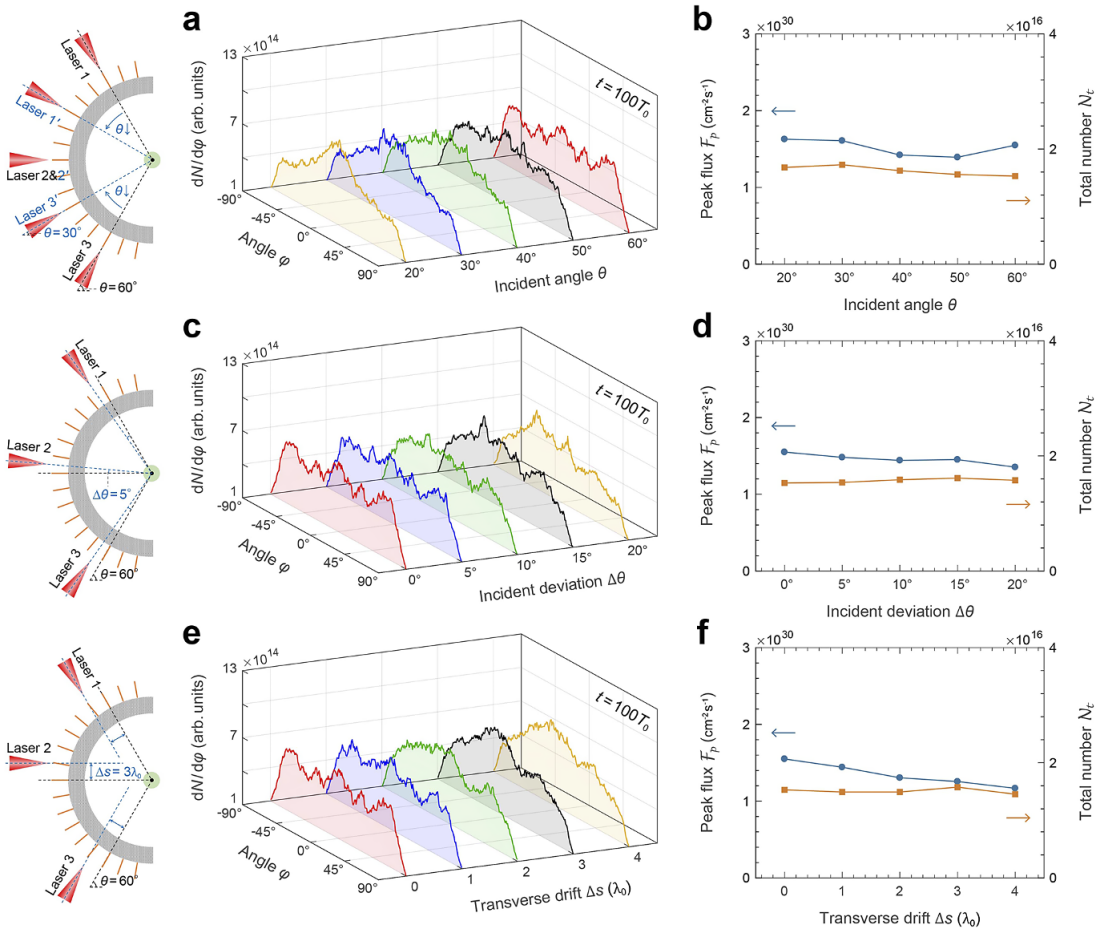


**Figure 7.** (a), (c), (e) Angular distribution and (b), (d), (f) peak flux $\mathcal{F}_\mathrm{p}$ (left) and total number $\mathcal{N}_\mathrm{t}$ (right) of the TNSA protons versus the laser incident angle $\theta$, misalignment $\Delta\theta$ of the laser incident angle and transverse drift $\Delta s$ of the focal spot. The panels on the far left are for $\theta = 30°$, with misalignment $\Delta\theta = 5°$ and transverse drift $\Delta s = 3\lambda_0$.

$P \leq 200$ TW, the density of the preplasma is usually below the critical plasma density. As $P$ continues to rise, the preplasma in most regions is over critical density, as shown in Figures 8(b) and 8(c). The density distributions from FLASH simulations are then imported into EPOCH code as the initial density distributions of the wire-hemisphere target. Figure 8(d) shows the dependence of $\mathcal{F}_\mathrm{p}$ on $P$ without and with preplasma. We find that the preplasma has little effect on $\mathcal{F}_\mathrm{p}$ as $P$ is less than 200 TW, since the preplasma has low enough density to be classically transparent. However, when $P$ is higher, the overcritical preplasma between the wires will block the channels and prevent laser injection, resulting in a dramatic reduction of $\mathcal{F}_\mathrm{p}$ by approximately 50%. This indicates that for high-contrast lasers with low energy and modest intensity, the effect of preplasma on proton acceleration in the proposed scheme is negligible. For long pulses of high-energy lasers, the contrast needs to be further improved to avoid ablation of the microstructure. The effect of preplasma at different values of $P$ on the angular distribution of protons is shown in Figure 8(e). We see that with increasing $P$, the angular distribution of the protons is more uniform, since the roughness of the periodic microstructure is diminished by the ablative effect of the stronger laser.

## 5. Summary

A practical scheme of producing high-flux and angularly uniform proton acceleration using three laser beams interacting with a wire-hemisphere target is proposed and demonstrated by PIC simulations. The peak proton flux and angular uniformity are significantly better than that from the traditional methods. The scheme can be useful for creating warm dense plasma states that are relevant to laboratory astrophysics[43], as well as fundamental material property[14] and controlled fusion[44] research. It should, however, be mentioned that we have invoked ultrashort relativistic laser pulses with duration of approximately 33 fs and energy of approximately 0.16 J per beam. For applications such as proton-beam-driven fast ignition of ICF, the protons must deposit sufficient energy (10–20 kJ) in a hot spot to ignite the fuel[45]. That is,

https://doi.org/10.1017/hpl.2024.55 Published online by Cambridge University Press

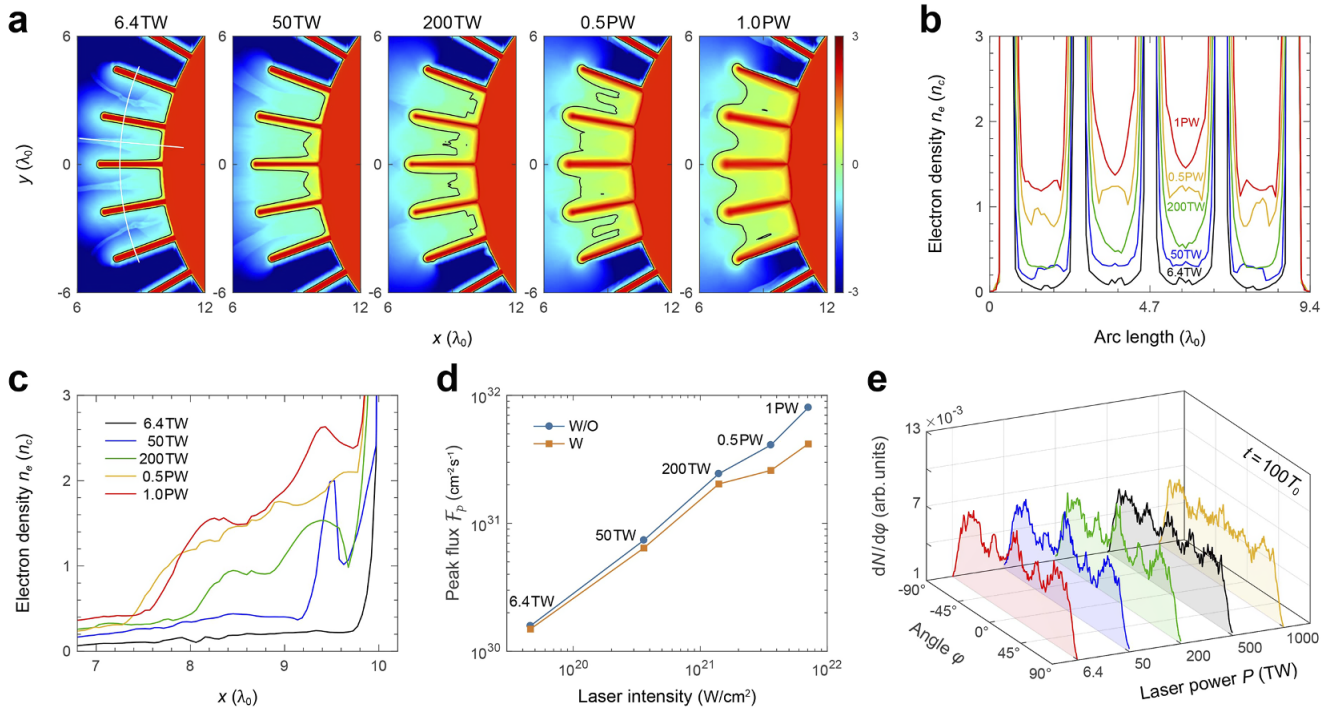


**Figure 8.** Results of radiation hydrodynamic simulations. (a) Density distribution of preplasma produced by the prepulse at different laser power $P$, and its (b) angular and (c) radial profiles along the white lines in (a). The density is in logarithmic color scale and these data are extracted 3 ps before the peak of the main pulse arrived. The black curves in (a) are the contour of the overcritical region. The above density distributions from FLASH simulations are then used in the PIC code EPOCH as input parameters of the wire-hemisphere target. Dependence of (d) the peak flux $\mathcal{F}_p$ and (e) angular distribution of protons on $P$ both without and with preplasma from the simulation.

long-pulse (a few ps) high-energy (hundreds of kJ) lasers are required. With such high-energy picosecond laser pulses, even with high contrast, microstructures such as that used here would be rapidly filled with overcritical plasma[24] that could distort the proton acceleration.

## Acknowledgements

This work was supported by the National Natural Science Foundation of China (Nos. 12105362, 12175310, 12275356 and 12305268), the Natural Science Foundation of Hunan Province (Nos. 2022JJ20042, 2021JJ40653 and 2020JJ5031), the Scientific Research Foundation of Hunan Provincial Education Department (No. 22B0655) and the Hunan Provincial Innovation Foundation for Postgraduate (No. CX20210006).

## References

1. J. Piekoszewski, Z. Werner, and W. Szymczyk, Vacuum **63**, 475 (2001).
2. G. E. Remnev, I. F. Isakov, M. S. Opekounov, G. I. Kotlyarevsky, V. L. Kutuzov, V. S. Lopatin, V. M. Matvienko, M. Yu. Ovsyagnikov, A. V. Potyomkin, and V. A. Tarbokov, Surf. Coat. Technol. **96**, 103 (1997).
3. D. J. Rej, H. A. Davis, J. C. Olson, G. E. Remnev, A. N. Zakoutaev, V. A. Ryzhkov, V. K. Struts, I. F. Isakov, V. A. Shulov, N. A. Nochevnaya, R. W. Stinnett, E. L. Neau, K. Yatsui, and W. Jiang, J. Vac. Sci. Technol. A **15**, 1089 (1997).
4. X. Y. Le, S. Yan, W. J. Zhao, B. X. Han, Y. G. Wang, and J. M. Xue, Surf. Coat. Technol. **128**, 381 (2000).
5. M. Koenig, A. Benuzzi-Mounaix, A. Ravasio, T. Vinci, N. Ozaki, S. Lepape, D. Batani, G. Huser, T. Hall, D. Hicks, A. MacKinnon, P. Patel, H. S. Park, T. Boehly, M. Borghesi, S. Kar, and L. Romagnani, Plasma Phys. Controll. Fusion **47**, B441 (2005).
6. A. B. Zylstra, O. A. Hurricane, D. A. Callahan, A. L. Kritcher, J. E. Ralph, H. F. Robey, J. S. Ross, C. V. Young, K. L. Baker, D. T. Casey, et al., Nature **601**, 542 (2022).
7. D. H. H. Hoffmann, V. E. Fortov, I. V. Lomonosov, V. Mintsev, N. A. Tahir, D. Varentsov, and J. Wieser, Phys. Plasmas **9**, 3651 (2002).
8. D. Strickland and G. Mourou, Opt. Commun. **55**, 447 (1985).
9. H. Daido, M. Nishiuchi, and A. S. Pirozhkov, Rep. Prog. Phys. **75**, 056401 (2012).
10. A. Macchi, M. Borghesi, and M. Passoni, Rev. Mod. Phys. **85**, 751 (2013).
11. A. X. Li, C. Y. Qin, H. Zhang, S. Li, L. L. Fan, Q. S. Wang, T. J. Xu, N. W. Wang, L. H. Yu, Y. Xu, Y. Q. Liu, C. Wang, X. L. Wang, Z. X. Zhang, X. Y. Liu, P. L. Bai, Z. B. Gan, X. B. Zhang, X. B. Wang, C. Fan, Y. J. Sun, Y. H. Tang, B. Yao, X. Y. Liang, Y. X. Leng, B. F. Shen, L. L. Ji, R. X. Li, and Z. Z. Xu, High Power Laser Sci. Eng. **10**, e26 (2022).
12. C. Y. Qin, H. Zhang, S. Li, S. H. Zhai, A. X. Li, J. Y. Qian, J. Y. Gui, F. X. Wu, Z. X. Zhang, Y. Xu, X. Y. Liang, Y. X. Leng, B. F. Shen, L. L. Ji, and R. X. Li, High Power Laser Sci. Eng. **10**, e2 (2022).
13. C. N. Danson, C. Haefner, J. Bromage, T. Butcher, J. F. Chanteloup, E. A. Chowdhury, A. Galvanauskas, L. A. Gizzi, J. Hein, D. I. Hillier, N. W. Hopps, Y. Kato, E. A. Khazanov, R. Kodama, G. Korn, R. X. Li, Y. T. Li, J. Limpert, J. G. Ma, C. H. Nam, D. Neely, D. Papadopoulos, R. R. Penman, L. J.

https://doi.org/10.1017/hpl.2024.55 Published online by Cambridge University Press

Qian, J. J. Rocca, A. A. Shaykin, C. W. Siders, C. Spindloe, S. Szatmári, R. M. G. M. Trines, J. Q. Zhu, P. Zhu, and J. D. Zuegel, High Power Laser Sci. Eng. **7**, e54 (2019).
14. G. W. Collins, L. B. Da Silva, P. Celliers, D. M. Cold, M. E. Foord, R. J. Wallace, A. Ng, S. V. Weber, K. S. Budil, and R. Cauble, Science **281**, 1178 (1998).
15. F. J. Rogers and C. A. Iglesias, Science **263**, 50 (1994).
16. M. Tabak, J. Hammer, M. E. Glinsky, W. L. Kruer, S. C. Wilks, J. Woodworth, E. M. Campbell, M. D. Perry, and R. J. Mason, Phys. Plasmas **1**, 1626 (1994).
17. M. Roth, T. E. Cowan, M. H. Key, S. P. Hatchett, C. Brown, W. Fountain, J. Johnson, D. M. Pennington, R. A. Snavely, S. C. Wilks, K. Yasuike, H. Ruhl, F. Pegoraro, S. V. Bulanov, E. M. Campbell, M. D. Perry, and H. Powell, Phys. Rev. Lett. **86**, 436 (2001).
18. P. K. Patel, A. J. Mackinnon, M. H. Key, T. E. Cowan, M. E. Foord, M. Allen, D. F. Price, H. Ruhl, P. T. Springer, and R. Stephens, Phys. Rev. Lett. **91**, 125004 (2003).
19. J. Badziak and S. Jabłoński, Appl. Phys. Lett. **90**, 151503 (2007).
20. T. Bartal, M. E. Foord, C. Bellei, M. H. Key, K. A. Flippo, S. A. Gaillard, D. T. Offermann, P. K. Patel, L. C. Jarrott, D. P. Higginson, M. Roth, A. Otten, D. Kraus, R. B. Stephens, H. S. McLean, E. M. Giraldez, M. S. Wei, D. C. Gautier, and F. N. Beg, Nat. Phys. **8**, 139 (2012).
21. H. Xu, W. Yu, M. Y. Yu, H. B. Cai, S. X. Luan, X. H. Yang, Y. Yin, H. B. Zhuo, J. W. Wang, C. T. Zhou, M. Murakami, and Z. Z. Xu, Appl. Phys. Lett. **104**, 024105 (2014).
22. C. McGuffey, J. Kim, M. S. Wei, P. M. Nilson, S. N. Chen, J. Fuchs, P. Fitzsimmons, M. E. Foord, D. Mariscal, H. S. McLean, P. K. Patel, R. B. Stephens, and F. N. Beg, Sci. Rep. **10**, 9415 (2020).
23. X. M. Li, Y. Chao, D. J. Liu, S. T. Zhang, Z. J. Liu, L. H. Cao, and C. Y. Zheng, J. Plasma Phys. **89**, 905890113 (2023).
24. M. Bailly-Grandvaux, D. Kawahito, C. McGuffey, J. Strehlow, B. Edghill, M. S. Wei, N. Alexander, A. Haid, C. Brabetz, V. Bagnoud, R. Hollinger, M. G. Capeluto, J. J. Rocca, and F. N. Beg, Phys. Rev. E **102**, 021201 (2020).
25. S. Jiang, L. L. Ji, H. Audesirk, K. M. George, J. Snyder, A. Krygier, P. Poole, C. Willis, R. Daskalova, E. Chowdhury, N. S. Lewis, D. W. Schumacher, A. Pukhov, R. R. Freeman, and K. U. Akli, Phys. Rev. Lett. **116**, 085002 (2016).
26. T. Ebert, R. Heber, T. Abel, J. Bieker, G. Schaumann, and M. Roth, High Power Laser Sci. Eng. **9**, e24 (2021).
27. P. J. Wang, G. J. Qi, Z. Pan, D. F. Kong, Y. R. Shou, J. B. Liu, Z. X. Cao, Z. S. Mei, S. R. Xu, Z. P. Liu, S. Y. Chen, Y. Gao, J. R. Zhao, and W. J. Ma, High Power Laser Sci. Eng. **9**, e29 (2021).
28. A. Jullien, S. Kourtev, O. Albert, G. Chériaux, J. Etchepare, N. Minkovski, and S. M. Saltiel, Appl. Phys. B **84**, 409 (2006).
29. Q. Chen, D. Maslarova, J. Z. Wang, S. X. Lee, V. Horný, and D. Umstadter, Phys. Rev. Lett. **128**, 164801 (2022).
30. B. Y. Li, F. Liu, M. Chen, F. Y. Wu, J. W. Wang, L. Lu, J. L. Li, X. L. Ge, X. H. Yuan, W. C. Yan, L. M. Chen, Z. M. Sheng, and J. Zhang, Phys. Rev. Lett. **128**, 244801 (2022).
31. T. D. Arber, K. Bennett, C. S. Brady, A. Lawrence-Douglas, M. G. Ramsay, N. J. Sircombe, P. Gillies, R. G. Evans, H. Schmitz, A. R. Bell, and C. P. Ridgers, Plasma Phys. Controll. Fusion **57**, 113001 (2015).
32. X. R. Jiang, D. B. Zou, Z. J. Zhao, L. X. Hu, P. Han, J. Q. Yu, T. P. Yu, Y. Yin, and F. Q. Shao, Phys. Rev. Appl. **15**, 034032 (2021).
33. D. Y. Yu, D. B. Zou, M. Y. Yu, T. P. Yu, Y. Yin, F. Q. Shao, H. B. Zhuo, C. T. Zhou, and S. C. Ruan, New J. Phys. **21**, 083003 (2019).
34. P. Mora, Phys. Rev. Lett. **90**, 185002 (2003).
35. J. L. Liu, M. Chen, J. Zheng, Z. M. Sheng, and C. S. Liu, Phys. Plasmas **20**, 063107 (2013).
36. A. Héron, J. C. Adam, and P. Mora, Phys. Plasmas **27**, 013103 (2020).
37. D. B. Zou, A. Pukhov, L. Q. Yi, H. B. Zhou, T. P. Yu, Y. Yin, and F. Q. Shao, Sci. Rep. **7**, 42666 (2017).
38. A. Curtis, C. Calvi, J. Tinsley, R. Hollinger, V. Kaymak, A. Pukhov, S. J. Wang, A. Rockwood, Y. Wang, V. N. Shlyaptsev, and J. J. Rocca, Nat. Commun. **9**, 1077 (2018).
39. D. F. Kong, G. Q. Zhang, Y. R. Shou, S. R. Xu, Z. S. Mei, Z. X. Cao, Z. Pan, P. J. Wang, G. J. Qi, Y. Lou, Z. G. Ma, H. Y. Lan, W. T. Wang, Y. H. Li, P. Rubovic, M. Veselsky, A. Bonasera, J. R. Zhao, Y. X. Geng, Y. Y. Zhao, C. B. Fu, W. Luo, Y. G. Ma, X. Q. Yan, and W. J. Ma, Matter Radiat. Extremes **7**, 064403 (2022).
40. X. R. Jiang, F. Q. Shao, D. B. Zou, M. Y. Yu, L. X. Hu, X. Y. Guo, T. W. Huang, H. Zhang, S. Z. Wu, G. B. Zhang, T. P. Yu, Y. Yin, H. B. Zhuo, and C. T. Zhou, Nucl. Fusion **60**, 076019 (2020).
41. B. Fryxell, K. Olson, P. Ricker, F. X. Timmes, M. Zingale, D. Q. Lamb, P. Macneice, R. Rosner, J. W. Truran, and H. Tufo, Astrophys. J. Suppl. Ser. **131**, 273 (2000).
42. J. J. MacFarlane, I. E. Golovkin, and P. R. Woodruff, J. Quant. Spectrosc. Radiat. Transfer **99**, 381 (2006).
43. B. A. Remington, D. Arnett, R. P. Drake, and H. Takabe, Science **284**, 1488 (1999).
44. J. Nuckolls, L. Wood, A. Thiessen, and G. Zimmerman, Nature **239**, 139 (1972).
45. S. Atzeni, A. Schiavi, J. J. Honrubia, X. Ribeyre, G. Schurtz, P. Nicolaï, M. Olazabal-Loumé, C. Bellei, R. G. Evans, and J. R. Davies, Phys. Plasmas **15**, 056311 (2008).

https://doi.org/10.1017/hpl.2024.55 Published online by Cambridge University Press